

Supporting Material
Structure of the SnO₂(110)-(4 × 1) surface

Lindsay R. Merte,^{1,*} Mathias S. Jørgensen,² Katariina Pussi,³ Johan Gustafson,¹ Mikhail Shipilin,¹ Andreas Schaefer,¹ Chu Zhang,¹ Jonathan Rawle,⁴ Chris Nicklin,⁴ Geoff Thornton,⁵ Robert Lindsay,⁶ Bjørk Hammer,² and Edvin Lundgren¹

¹*Division of Synchrotron Radiation Research,
Lund University, 22 100 Lund, Sweden*

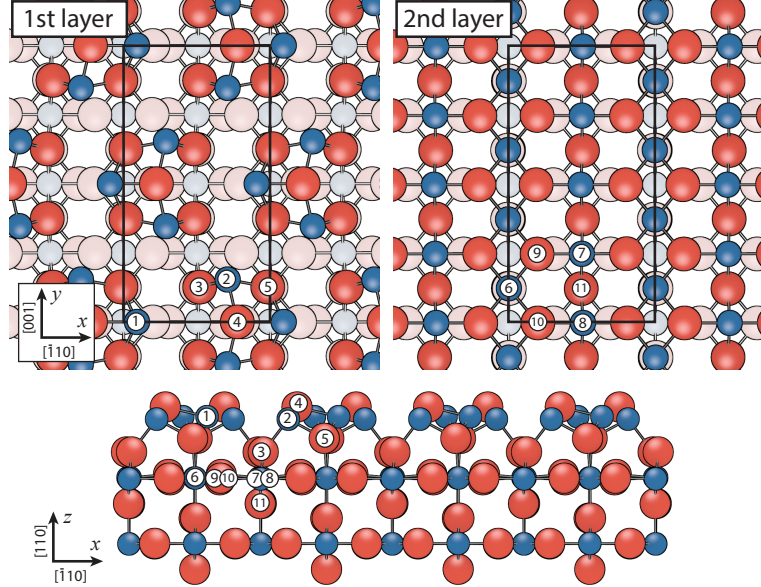
²*Interdisciplinary Nanoscience Center (iNANO)
and Department of Physics and Astronomy,
Aarhus University, DK-8000 Aarhus C, Denmark*

³*LUT School of Engineering Science,
P.O. Box 20, FIN-53851 Lappeenranta, Finland*

⁴*Diamond Light Source, Harwell Science and Innovation Campus, Didcot OX11 0DE, UK*

⁵*Department of Chemistry and London Centre for Nanotechnology,
University College London, London WC1H 0AJ, United Kingdom*

⁶*Corrosion and Protection Centre, School of Materials,
The University of Manchester, Sackville Street, Manchester M13 9PL, UK*



Atom ID	Element	<i>x</i>	<i>y</i>	<i>z</i>
1	Sn	0.092	0.000	0.464
2	Sn	0.710	0.153	0.453
3	O	0.520	0.126	0.198
4	O	0.776	0.000	0.540
5	O	0.983	0.126	0.298
6	Sn	0.003	0.125	-0.002
7	Sn	0.500	0.250	-0.007
8	Sn	0.508	0.000	0.000
9	O	0.195	0.249	0.003
10	O	0.200	0.000	0.026
11	O	0.496	0.124	-0.191

TABLE I. Atomic coordinates determined for the (4×1) structure by DFT and LEED, given for symmetrically inequivalent (group $p2mg$) atoms belonging to the overlayer and the uppermost SnO_2 trilayer. Fractional coordinates are given with respect to the (4×1) unit cell shown, where x lies along $[\bar{1}10]$, y along $[001]$ and z along $[110]$. In-plane (x, y) coordinates are those determined by DFT calculations while out of plane (z) coordinates are the result of the fit to the LEED IV data. For simulation of the LEED measurements unit cell dimensions of $(6.69\text{\AA} \times 12.72\text{\AA} \times 6.69\text{\AA})$ were assumed. The optimized unit cell applied in the DFT calculations was about $\sim 3\%$ larger, at $(6.9\text{\AA} \times 13.0\text{\AA} \times 6.9\text{\AA})$. The edges of the unit cell coincide with mirror planes of the bulk SnO_2 crystal structure.

SXRD MEASUREMENTS

Experimental details

The experiment was conducted using the large UHV system installed in Experimental Hutch 2, beamline I07 at the Diamond Light Source [1]. This system is composed of two connected chambers, one for sample preparation and preliminary characterization, and one with the hexapod diffractometer stage and a beryllium window for analysis of the sample by X-ray diffraction. The preparation chamber was equipped with an ion gun for Ar^+ sputtering and a LEED optics. The manipulator was equipped with a filament for radiative sample heating and a thermocouple measuring the temperature at the back of the sample holder. The entire chamber was mounted in a six-circle diffractometer such that the sample surface normal was oriented horizontally. A fixed beam energy of 18 keV was used. The scattered X-rays were detected using a Pilatus 100K 2-dimensional detector.

The sample, provided by SurfaceNet GmbH, was a natural cassiterite crystal, cut to 8 mm \times 8 mm \times 1 mm and polished on the (110) face. The crystal was mounted to a Ta sample plate using Ta wires pressed over two of the corners (see Fig. 1(a)). The sample was cleaned by Ar^+ sputtering and annealing. As the apparatus did not permit direct measurement of the sample temperature, annealing was performed by fixing the heating power at a particular value for a set amount of time and monitoring the temperature of the sample plate using an optical pyrometer. As discussed by Batzill [2], the (4 \times 1) phase can be prepared by annealing the sputtered surface at a temperature between ca. 1000 K and 1200 K. At lower temperatures a $c(2 \times 2)$ phase is present while at higher temperatures the (4 \times 1) phase decomposes to form first a disordered phase (showing a (1 \times 1) pattern in LEED) and then a (1 \times 2) structure. By trial and error, heating settings were found that produced a surface exhibiting a clear (4 \times 1) pattern in LEED (Fig. 1(b)). The temperature measured on the sample plate for this preparation was 1200 K. After preparation, the sample was transferred to the diffractometer for SXRD measurements, which were performed with the sample at room temperature. In-plane SXRD survey scans show the characteristic features of the (4 \times 1) structure, and are plotted in Fig. 1(c,d). These measurements were made by scanning along the K direction, keeping H and L fixed. The plotted intensity is the integrated signal from a region of interest at the center of the detector during this scan.

SXRD measurements were made with a fixed incident angle of 0.2°. The majority of the diffraction signals from the (4 \times 1) structure were very weak, and this low incident angle was chosen to enhance the signal-to-noise ratio; the weak reflections were undetectable otherwise. At this angle, the beam footprint on the sample was estimated to be approximately 8 mm long, so that the measurements are sensitive to inhomogeneity and to slight sample misalignment. Comparison of symmetrically-equivalent diffraction rods was used to estimate the magnitude of these effects, and based on this we estimate an upper limit to the uncertainty in the structure factors of $\sim 20\%$. Out-of-plane structure factors were measured by scanning in the L direction along different rods. The intensity above the background at each point was extracted by fitting a Gaussian-Lorentzian peak to the intensity profile at the center of the detector. In-plane structure factors were measured at a fixed L value of

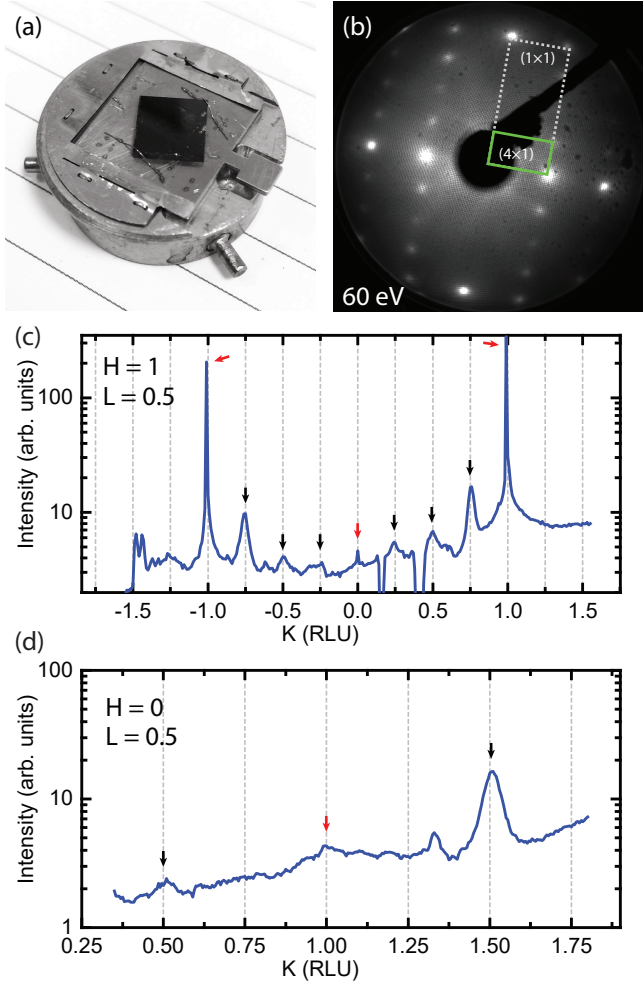


FIG. 1. (a) Photograph of the SnO₂ crystal fixed to the transferrable sample plate used for the SXRD measurements. (b) LEED pattern obtained after sample preparation by sputtering and annealing, showing the (4×1) periodicity. (c) In-plane SXRD scan in the K direction at $H=1$, $L=0.5$. (d) In-plane SXRD scan in the K direction at $H=0$, $L=0.5$. Dashed lines indicate positions corresponding to the (4×1) unit cell. Black arrows indicate fractional-order peaks corresponding to the SnO overlayer, while red arrows indicate bulk crystal truncation rods. Note the logarithmic intensity scale.

0.5 by rotating the sample with the detector held stationary (producing a so-called “rocking curve”). The intensities of the resulting profiles were determined by peak fitting [3]. Values proportional to structure factors were produced after modification of the raw intensities by the beam polarization, Lorentz distortion and rod interception correction factors, as discussed by Vlieg [4]. The detector was wide enough that the entire widths of the rods could be integrated, and the slits were set wide enough that the entire beam footprint on the sample was visible.

Simulation of SXRD structure factors and fitting of various models to the experimental data was performed using the program ROD by Elias Vlieg [5] and WINROD by Daniel Kaminski [6]. For the fits, different scale parameters were used for integer- and non-integer

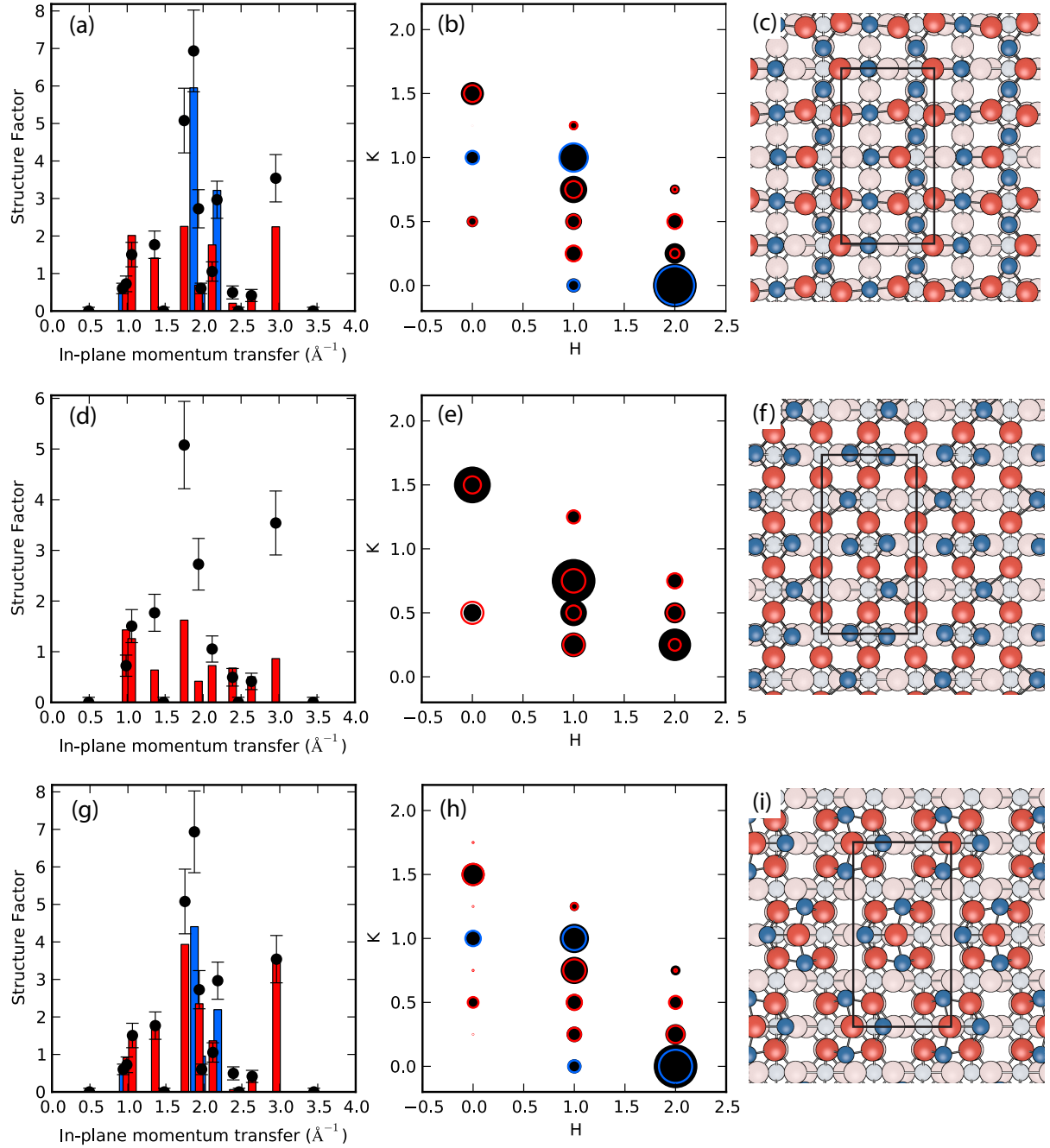


FIG. 2. (a,b) Comparison of experimental and calculated structure factors for the in-plane vacancy model of Atrei et al. In (a) these are plotted in one dimension as a function of in-plane momentum transfer, while in (b) these are shown as discs with radius proportional to structure factor at their respective positions in reciprocal space. In both, experimental values are plotted in black, while red bars/circles correspond to fitted values for fractional-order superstructure rods and blue bars/circles to fitted values for integer-order crystal truncation rods. (c) shows a ball model of the structure used. (d,e,f) show similar plots for the “interstitial” model of Batzill et al. (g,h,i) show the results for our proposed model, for comparison.

rods to account for differences in the intensities caused by e.g. incomplete coverage or disorder in the overlayer as well as a significant difference in peak profile. A Debye-Waller parameter of 5 was used, corresponding to a RMS displacement of ~ 0.2 Å, which includes the effects of both static and dynamic disorder. For fits where atomic positions were optimized, the positions were parametrized such that the observed *p2mg* symmetry was obeyed. Error bars for all rods were fixed at 20% of the measurement magnitude.

Atrei and Batzill models

Simulated structure factors for the in-plane vacancy model as proposed by Atrei et al. [7] and the “interstitial” model introduced by Batzill et al. [8] are compared to experimental ones in Fig. 2. In the case of the in-plane vacancy model (Fig. 2(a-c)), the coordinates were fixed to those found by Atrei et al. from LEED I(V) fits. The creation of two vacancies leaves behind six oxygen atoms that, if allowed to form a hexagonal arrangement, can produce an in-plane diffraction pattern qualitatively similar to that formed by Sn atoms in the Sn_6O_6 structure we found. Such an arrangement is not compatible with LEED or DFT structure refinement, however, and would be expected to produce diffraction features at least an order of magnitude weaker than those we observed. In the case of the Batzill model, atoms were allowed to relax laterally, but the fit to the data was very poor, with no clear optimum structure emerging. The fit to the structure shown in Fig. 2(d-f) includes only the fractional-order rods. With inclusion of integer-order rods the fit was notably worse.

LEED MEASUREMENTS

Experimental details

LEED I(V) measurements were undertaken in a UHV chamber (base pressure $\sim 1 \times 10^{-10}$ mbar), equipped with facilities for sample cleaning, cooling, and characterization. A commercial low-current (nA regime) LEED optics (MCP-LEED, OMICRON), which is fitted with a channel plate for image intensification, was employed for data acquisition.

The $\text{SnO}_2(110)$ sample was prepared *in situ* by cycles of Ar^+ sputtering and annealing. To form the (4×1) reconstruction, annealing at ~ 950 K was employed. This temperature was measured using a thermocouple attached to the plate upon which the sample was mounted. Surface order and cleanliness were determined by LEED and Auger electron spectroscopy, respectively.

LEED I(V) measurements were performed with the sample at ~ 180 K. To minimize surface contamination, the sample was flashed to ~ 570 K just prior to data collection. Auger spectra were never recorded directly before collecting LEED I(V) data, due to the possibility of electron beam induced surface damage. Data acquisition involved recording a series of LEED patterns as a function of the incident electron beam energy at 2 eV intervals over the range 40 eV – 300 eV. A CCD camera, interfaced to a computer, was employed for image capture. For the LEED I(V) measurements the incident electron beam

was essentially normal to the surface. This geometry was achieved by comparing nominally symmetry-equivalent diffraction beams.

For the structure determination, so-called IV-curves (i.e. plots of diffracted beam intensity (I) versus electron beam energy) were generated from the data set of LEED patterns. At each electron beam energy, the total intensity (I_T) of an individual diffracted beam was extracted from the LEED pattern, using a software package, by summing the pixel intensity within a square encompassing the beam. A background (I_B), which was estimated from the intensity at the edges of the square, was then subtracted to obtain I , i.e. $I = I_T - I_B$. Following this procedure, IV-curves were compiled for 8 non-equivalent integral order beams, and 7 non-equivalent fractional order beams. The total energy range of these data is 1800 eV.

Determination of the surface geometry from the IV-curves involved the usual trial-and-error methodology of generating simulated IV-curves for a model structure, and then iteratively optimizing the geometry to find the best fit between experiment and theory as measured using the Pendry reliability factor (R_P) [9]. The Barbieri/Van Hove Automated Tensor LEED code was employed for the simulations [10, 11]. Nine phase shifts were used to describe the scattering. The imaginary part of the inner potential was set to -3 eV and the real part of the inner potential was assumed to be energy independent and allowed to vary to obtain the optimal value. The Debye temperatures used for surface and subsurface O were 400 K and 1100 K, respectively, and for surface and subsurface Sn 160 K and 400 K, respectively.

DFT CALCULATIONS

Computational details

A systematic density functional theory (DFT) search for atomic structures was performed with an evolutionary algorithm (EA) [12, 13] that is currently implemented in the Atomic Simulation Environment (ASE) [14] software. The starting structures for the EA were modeled with one fixed bottom layer of $\text{SnO}_2(110)$ and another layer of randomized atomic positions in a (4×1) unit cell with a grid of $(2 \times 2 \times 1)$ k -points and periodic boundaries in the x - and y -directions. The bridging oxygens O_{br} in the bottom layer are included in the group of randomized atoms to allow for subsurface reduction. The randomized overlayer consists of 0.75 ML Sn and four different O coverages: 0.25, 0.5, 0.75, and 1.0 ML. In the unit cell, this amounts to Sn_6O_2 , Sn_6O_4 , Sn_6O_6 , and Sn_6O_8 overlayers. The EA proceeds with the cut-and-splice pairing operator [15] followed by 30% probability of either a rattle mutation or a permutation mutation [13].

All structures are optimized with DFT within the grid-based projector-augmented wave (GPAW) method [16] using the PBE functional [17]. EA structures are optimized with a linear combination of atomic orbitals (lcao) until all forces are below 0.05 eV/Å. Global minimum structures are re-optimized with the finite-difference mode, a grid of $(3 \times 3 \times 1)$ k -points, and a four-layer slab (including the overlayer) until all forces are below 0.025 eV/Å. With 8 Å of vacuum below and above the slab and the optimized lattice parameters $a = 4.88$ Å and $c = 3.25$ Å, this results in a $(13.0 \times 6.9 \times 29.0)$ Å unit cell.

Four EA searches were run for each overlayer stoichiometry. A run is stopped when a better candidate structure has not been found for at least a few hundred attempts. Out of those runs, the global minimum was found once for Sn_6O_2 , twice for Sn_6O_4 , and all four times for Sn_6O_6 and Sn_6O_8 . On average, 383 unique structures (i.e. not counting duplicate candidate structures) were locally optimized in each EA run resulting in a total of 6125 unique structures for the entire search, of which 961 are unique Sn_6O_6 structures.

Phase diagram

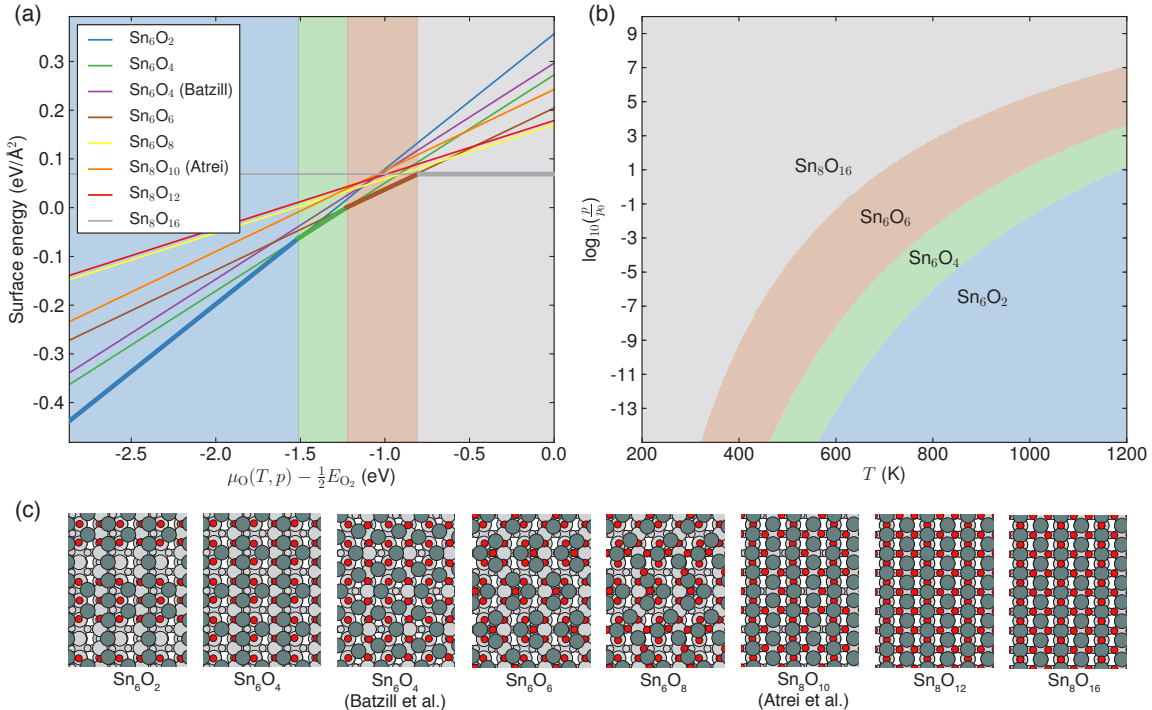


FIG. 3. (a) Surface energies of the globally optimized Sn_6O_y overlayers, the bulk terminated and slightly reduced overlayers, Sn_8O_{16} and Sn_8O_{12} , and the Batzill and Atrei models as a function of oxygen chemical potential. (b) Most stable overlayers as a function of pressure and temperature, where $p_0 = 1 \text{ atm}$. (c) The atomic structures with all atoms included in the EA search highlighted in color.

To assess the stability of the globally optimized Sn_6O_6 overlayer, all overlayers including the bulk termination, an overlayer with bridging oxygens removed, the Batzill model [8], and the Atrei model [7] are compared in a phase diagram (Fig. 3). Diagram (a) is constructed as outlined in Ref. [18] with the surface energy as a function of the oxygen chemical potential, where the lower limit ($\min[\mu_O(T, p)] = -2.87 \text{ eV}$) corresponds to decomposition into solid Sn and oxygen gas and the upper limit ($\max[\mu_O(T, p)] = 0 \text{ eV}$) corresponds to oxygen gas condensing on the surface. The bulk termination is stable from the upper limit down to $\mu_O(T, p) = -0.8 \text{ eV}$. While the Sn_6O_8 overlayer is not stable at any reduced condition,

the Sn_6O_6 overlayer is favored at oxygen chemical potentials from $\mu_O(T, p) = -0.8$ eV to $\mu_O(T, p) = -1.2$ eV. Diagram (b) shows the most stable overlayer as a function of pressure and temperature. While very accurate conclusions cannot be drawn from this diagram because the O_2 molecule is not very well described by DFT, the diagram suggests that the Sn_6O_6 overlayer is thermodynamically stable at ambient O_2 conditions at elevated temperatures of around 600-900 K. The atomic structures are shown in (c), where all atoms included in the EA search (the overlayer plus four subsurface oxygen atoms from bridge sites) are highlighted in color. Note that reduction only occurs in the overlayer of the Sn_6O_6 structure since all subsurface oxygen sites are occupied. The Batzill model and the Atrei model are not stable at any chemical potential in agreement with DFT calculations by Ágoston and Albe [19] showing both models to be unstable. Also, the Sn_6O_4 EA search resulted in 108 unique structures more stable than the Batzill model.

PDOS analysis

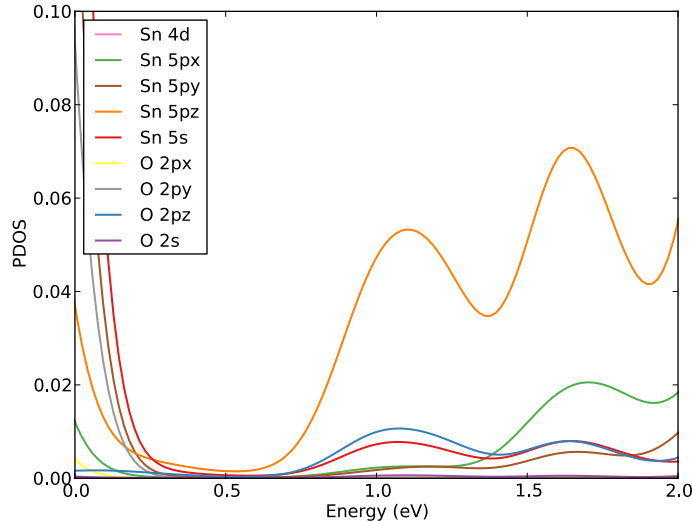


FIG. 4. Plots of the projected density of states (PDOS) calculated for various atomic orbitals for the outermost Sn and O atoms of the Sn_6O_6 structure. Energies are given with respect to the calculated Fermi level of the slab. The density of unoccupied states is dominated by Sn $5p_z$ orbitals.

Figure 4 shows the density of electronic states as a function of energy, projected onto atomic orbitals, for the outermost Sn and the apex O atom of the Sn_6O_6 structure. This shows that the most significant electronic states contributing to the unoccupied DOS, and thus to the formation of STM images at positive bias, are the Sn $5p_z$ orbitals. These states dominate over the weaker O $2p_z$ states, giving rise to the appearance of holes above apex O atoms.

Figure 5 shows the density of states projected onto a single stoichiometric surface layer, a single layer with a Sn_3O_3 overlayer, a single layer with a Sn_6O_6 overlayer, and a single

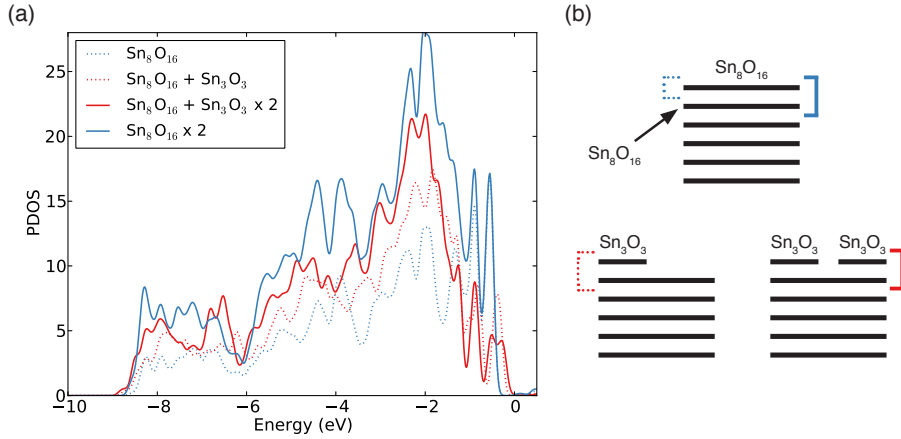


FIG. 5. (a) Plots of the density of states projected onto a single stoichiometric surface layer, a single layer with a Sn_3O_3 overlayer, a single layer with a Sn_6O_6 overlayer, and a single layer with a Sn_8O_{16} overlayer. Energies are given with respect to the calculated Fermi level of the slab. (b) Schematics of the layers onto which the density of states is projected.

layer with a Sn_8O_{16} overlayer. Schematics of these layers are shown in (b). These PDOS calculations are carried out on fully relaxed six-layer slabs with a grid of $(8 \times 8 \times 1)$ k -points. The Sn_3O_3 overlayer is similar to the Sn_6O_6 overlayer, but with one less isolated Sn_3O_3 cluster per unit cell. Thus one can analyze how the Sn_3O_3 clusters affect the electronic states of the surface. It is evident that a small band gap remains, and that the total density of states is similar to the stoichiometric (1×1) surface. This is consistent with previous photoemission measurements by Batzill et al. [20]

* lindsay.merte@sljus.lu.se

- [1] C. Nicklin, T. Arnold, J. Rawle, A. Warne, *J. Synchrotron Rad.* **2016**, *23*, 1245–1253.
- [2] M. Batzill, *Sensors* **2006**, *6*, 1345–1366.
- [3] J. Drnec, T. Zhou, S. Pintea, W. Onderwaater, E. Vlieg, G. Renaud, R. Felici, *J. Appl. Crystallogr.* **2013**, *47*, 365–377.
- [4] E. Vlieg, *J. Appl. Crystallogr.* **1997**, *30*, 532–543.
- [5] E. Vlieg, *J. Appl. Crystallogr.* **2000**, *33*, 401–405.
- [6] ANA-ROD project homepage at ESRF. http://www.esrf.eu/computing/scientific/joint_projects/ANA-ROD/.
- [7] A. Atrei, E. Zanazzi, U. Bardi, G. Rovida, *Surf. Sci.* **2001**, *475*, L223–L228.
- [8] M. Batzill, K. Katsiev, U. Diebold, *Surf. Sci.* **2003**, *529*, 295–311.
- [9] J. B. Pendry, *J. Phys. C: Solid State Phys.* **1980**, *13*, 937.
- [10] M. A. Van Hove, W. Moritz, H. Over, P. J. Rous, A. Wander, A. Barbieri, N. Materer, U. Starke, G. A. Somorjai, *Surf. Sci. Rep.* **1993**, *19*, 191 – 229.
- [11] A. Barbieri, M. A. Van Hove. <http://www.ap.cityu.edu.hk/personal-website/Van-Hove>.

htm.

- [12] L. B. Vilhelmsen, B. Hammer, *Phys. Rev. Lett.* **2012**, *108*, 126101.
- [13] L. B. Vilhelmsen, B. Hammer, *J. Chem. Phys.* **2014**, *141*, 044711.
- [14] S. R. Bahn, K. W. Jacobsen, *Comput. Sci. Eng.* **2002**, *4*, 56–66.
- [15] D. M. Deaven, K. M. Ho, *Phys. Rev. Lett.* **1995**, *75*, 288–291.
- [16] J. J. Mortensen, L. B. Hansen, K. W. Jacobsen, *Phys. Rev. B* **2005**, *71*, 035109.
- [17] J. P. Perdew, K. Burke, M. Ernzerhof, *Phys. Rev. lett.* **1996**, *77*, 3865.
- [18] K. Reuter, M. Scheffler, *Phys. Rev. B* **2001**, *65*, 035406.
- [19] P. Ágoston, K. Albe, *Surf. Sci.* **2011**, *605*, 714–722.
- [20] M. Batzill, K. Katsiev, J. M. Burst, U. Diebold, A. M. Chaka, B. Delley, *Phys. Rev. B* **2005**, *72*, 165414.